Hole Fermi surface in Bi_{2}Se_{3} probed by quantum oscillations

B. A. Piot, W. Desrat, D. K. Maude, M. Orlita, M. Potemski, G. Martinez, and Y. S. Hor

Phys. Rev. B **93**, 155206 — Published 27 April 2016

DOI: 10.1103/PhysRevB.93.155206

The hole Fermi surface in Bi_2Se_3 probed by quantum oscillations

B. A. Piot[1], W. Desrat [2], D.K. Maude[3], M. Orlita[1], M. Potemski[1], G. Martinez[1]
[1] *Laboratoire National des Champs Magnétiques Intenses,*
LNCMI-CNRS-UGA-UPS-INSA-EMFL, F-38042 Grenoble, France
[2]*Université Montpellier 2 and CNRS, Laboratoire Charles Coulomb (L2C),*
UMR 5221 CNRS-Université de Montpellier, F-34095 Montpellier, F-France and
[3] *Laboratoire National des Champs Magnétiques Intenses,*
LNCMI-CNRS-UGA-UPS-INSA-EMFL, F-31400 Toulouse, France

Y.S. Hor[4]
[4] *Department of Physics, Missouri University of Science and Technology, Rolla, MO 65409, USA*
(Dated: April 6, 2016)

Transport and torque magnetometry measurements are performed at high magnetic fields and low temperatures in a series of p-type (Ca-doped) Bi_2Se_3 crystals. The angular dependence of the Shubnikov-de Haas and de Haas-van Alphen quantum oscillations enables us to determine the Fermi surface of the bulk valence band states as a function of the carrier density. At low density, the angular dependence exhibits a downturn in the oscillations frequency between 0° and 90°, reflecting a bag-shaped hole Fermi surface. The detection of a single frequency for all tilt angles rules out the existence of a Fermi surface with different extremal cross-sections down to 24 meV. There is therefore no signature of a camel-back in the valence band of our bulk samples, in accordance with the direct band gap predicted by *GW* calculations.

PACS numbers: 71.18.+y,71.20.Nr,72.20.My

I. INTRODUCTION

Bi_2Se_3 is a narrow gap layered semiconductor which together with Bi_2Te_3 have been studied for decades for their thermo-electric properties.[1] The interest in this class of materials has recently surged because of the prediction[2] and observation[3,4] of a unique type of charge carriers existing at their surface, the so-called "helical Dirac fermions", which behave as massless relativistic particles with a spin locked to their translational momentum. Bi_2Se_3 therefore now belongs to the 3D topological insulators family characterized by a bulk gap coexisting with 2D conducting surface states. As a matter of fact, the existence of gapless states at the boundary of the material is related to a well defined change in the *bulk* band structure. In Bi_2Se_3, this originates from a parity inversion of the valence and conduction bands at the Γ point of the Brillouin zone in the presence of a large spin orbit coupling.[2,5] The linear-in-momentum dispersion relation which characterizes the 2D surface states thus emerges from the general Hamiltonian of massive Dirac fermions,[2] theoretically expected to describe the bulk states in Bi_2Se_3.

Pioneering experimental studies of the bulk conduction band at low energy[6] have reported an ellipsoidal electron Fermi surface, which was described within a simple model of massive carriers with a parabolic (non-parabolic) dispersion in the $k_\perp$ ($k_\parallel$) direction, where $k_\perp$ ($k_\parallel$) is the momentum in the direction perpendicular (parallel) to the *c*-axis of the crystal. This is accompanied by an increasing anisotropy of the Fermi surface observed as the Fermi level increases in the conduction band. More recent transport,[7–9] NMR,[9] and magneto-optics[10] measurements have confirmed the original parameters phenomenologically describing the bulk conduction band, and in some cases[10] connected them to the 3D Dirac Hamiltonian for massive fermions applied to topological insulators.

However, experimental studies of the *valence band* bulk Fermi surface are to our knowledge scarce. The principal reason is that as-grown Bi_2Se_3 is electron-doped due to the presence of Se vacancies. The discovery of 2D surface states has nevertheless triggered large efforts to reach the topological insulator regime, where the Fermi level lies in the band gap of the bulk band structure. For instance, substituting trace amounts of Ca^{2+} for Bi^{3+} in as-grown Bi_2Se_3 can lower the Fermi energy of the native n-type crystals. Above a certain value of Ca-doping δ, the electrical conduction in $Bi_{2-\delta}Ca_\delta Se_3$ is supported by hole carriers rather than electrons.[11,12] Further doping brings the Fermi level deep in the previously inaccessible valence band. Very recently, Shubnikov-de Haas (SdH) measurements have been reported[13] in p-type Bi_2Se_3 samples with hole concentrations estimated between 5.7×10^{18} cm^{-3} and 1.6×10^{19} cm^{-3}. A bag-like closed Fermi surface was observed at low concentration, with the suggestion of open tubes appearing in the Fermi surface at high carrier density. In spite of these first experimental advances, and several theoretical works,[1,2,14,15] the low-energy details of the valence band are still not unambiguously determined. In particular, a local minimum was suggested to form at the Γ point as a consequence of the spin-orbit coupling. While a camel-back structure is observed in the valence band near the surface,[12] it is absent in some bulk measurements.[10,16,17] More recent *GW* calculations[18,19] show that the electron-electron interactions reduce the band gap at the Γ point and wash out the camel-back structure. This issue brings further motivation to experimentally investigate the bulk valence band, in particular close to the Γ point.

In this article, we present a doping dependent study of the bulk valence band Fermi surface in Bi_2Se_3 in a previously unexplored low energy range. High quality calcium-doped Bi_2Se_3 crystals are studied by magneto-transport and torque magnetometry at low temperatures and under magnetic fields up to 30 T. A high resolution angular dependence of the quantum oscillations (both Shubnikov-de Haas (SdH) and de Haas-van Alphen (dHvA)) enables us to map out the Fermi surface of the bulk valence band states, in the energy range $E_F \sim$ 20-60 meV. At low Fermi energies, a downturn is observed in the angular dependence of the oscillations frequency between 0° and 90°, demonstrating a bag-shaped closed Fermi surface. Importantly, a single frequency dominates the FFT spectra regardless of the magnetic field orientation, showing that no camel-back structure is observed for energies down to ∼ 24 meV. The existence of a camel-back structure for lower energies is hardly probable in respect to the experimental $E(k)$ dependence, which points to a direct band gap. The Fermi surface anisotropy increases rapidly as the Fermi level goes higher in the valence band, and pipe-like structures previously reported at high energy are confirmed and attributed to trigonal warping. The apparent hole effective mass, defined in the parabolic band approximation, is obtained by temperature-dependent studies for $B \parallel c$-axis, and lies in the $0.245 \pm 0.015\, m_0$ range for $E_F \sim 23 - 45$ meV. High magnetic fields measurement in the lowest density samples enable us to approach the quantum limit for holes which is finally discussed.

II. QUANTUM OSCILLATIONS IN P-TYPE Bi_2Se_3

A. Experimental details

The $Bi_{2-\delta}Ca_{\delta}Se_3$ samples studied here were grown via a process of two-step melting described in Ref. 11. By adding Ca, a transition to a p-type behavior is observed for x> 0.012,[20] which is the regime our study focuses on. The samples presented here are referred to as B2, B3, B6, E2, and E1, and their main characteristics are summarized in Table I.[21] Magneto-transport experiments were conducted on μm-thick slices on which silver paste contacts were deposited in a Hall bar-like or Van der Pauw configuration. Measurements were performed using a standard low frequency lock-in technique in a variable temperature insert for temperatures ranging from 1.2 K to 40 K, up to magnetic fields of 30 T produced by a 20 MW resistive magnet. The data were initially symmetrized by changing the polarity of the magnetic field to check that contact misalignment had a negligible impact on the analysis (notably the oscillation frequency). For dHvA torque measurements, samples of thickness varying between 40 and 230 μm were mounted on a CuBe cantilever which forms the mobile plate of a capacitive torque meter. The torque signal was measured with a lock-in amplifier and a capacitance bridge using conventional phase sensitive detection at 5.3 kHz. The experiment was performed using a 16 T superconducting magnet and a dilution fridge, equipped with an *in-situ* rotation stage. The torque measurements, which typically probe a larger number of particles, were employed to further confirm the domination of the bulk states in the present study.

	Ca doping (δ)	Expt	F (T)	m_h (m_0)	E_F (meV)
B2	0.015	SdH	48.7	0.238(0.01)	23.7
B3	0.015	SdH	55.8	-	27.15
B6	0.015	dHvA	87.8	-	-
B1	0.015	SdH	96	0.248(0.01)	44.8
D1	0.025	SdH	97	0.249(0.01)	45.1
E2	0.03	dHvA	100.8	-	46.9
E1	0.03	dHvA	126	-	58.6

TABLE I: Parameters of the Bi_2Se_3 samples. Calcium doping level δ defined by $Bi_{2-\delta}Ca_{\delta}Se_3$, experimental technique used, quantum oscillation main frequency, apparent valence band effective mass (m_h) and Fermi energy in the parabolic band approximation.

B. Magnetic field dependence

Figure 1 shows representative quantum oscillations in the valence band for the two extreme carrier densities studied. In Fig. 1(a), we report on magneto-transport (SdH) data on sample B3, one of our lowest density samples. Superimposed on a large monotonic background, oscillations of the resistivity reflect the oscillatory density of states of the system. The data in the upper left inset are obtained by subtracting a smoothed (moving window average) data curve. The resulting FFT is shown in the bottom right inset. It shows a clear single peak at about 55 T, consistent with the apparent absence of splitting in the data.

dHvA oscillations are shown for a sample with a higher carrier concentration (sample E1) in Fig. 1(b), where the torque signal τ is plotted as a function of the total magnetic field for a tilt angle $\theta = 16°$. Small quantum oscillations in τ, again on a large monotonous background, are clearly visible and reflect the oscillatory magnetization of the system. The dHvA oscillations can be better observed in the oscillatory torque ($\Delta\tau$), obtained with the same background removal procedure as for transport. Here also a single frequency is observed, at a higher value consistent with the higher carrier concentration of sample E1. We note that the results obtained with the two different experimental techniques for a given carrier density are fully consistent.

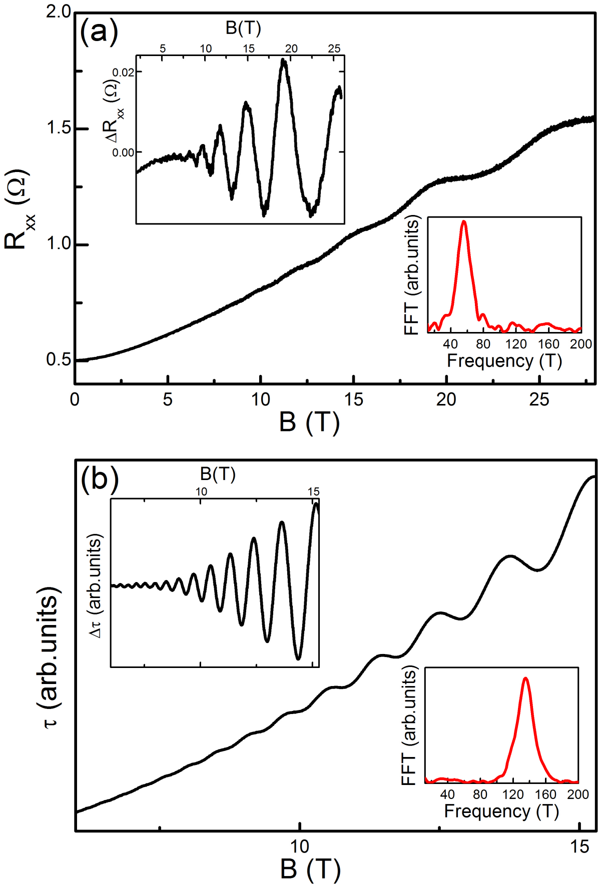

FIG. 1: (color online) (a) Longitudinal resistance R_{xx} versus total magnetic field in perpendicular configuration for a low-doped p-type Bi_2Se_3 sample (B3) at $T = 1.2$ K. Upper left inset: oscillatory resistance ΔR_{xx}. Lower right inset: fast Fourier transform of $\Delta R_{xx}(1/B)$. (b) Torque τ and oscillatory torque $\Delta\tau$ (lower right inset) versus total magnetic field for $\theta = 16°$ in a highly-doped p-type Bi_2Se_3 sample (E1). (Upper left inset) Fourier transform of $\tau(1/B\cos\theta)$.

C. Temperature dependence

The temperature dependence of the SdH oscillations was measured for samples B1, D1, B2 and B3 between 1.3 K and 40 K for magnetic fields up to 30 T. In Fig. 2, we report typical results obtained on samples B1 and B2 up to 11 T, for temperatures between 1.3 K and 25 K. In the upper left inset, we plot the temperature dependence of the oscillation amplitude at the fixed magnetic field $B = 9.6$ T. The same type of data are reported in the lower-left inset for a lower concentration sample (B2) at a similar magnetic field ($B = 10.6$ T). The amplitude of the oscillations has not fully saturated at $T = 1.3$ K, suggesting a higher hole effective mass compared to the well-documented n-type samples[6,9] in qualitative agreement with recent magneto-optics studies.[10] The temperature damping of the oscillations can be well-described by the standard Lifshitz-Kosevich formalism[22], valid in this case of 3D quantum oscillations of moderate amplitude. We extract the energy gap Δ, from which the apparent effective mass of holes is defined, $m_h = (\hbar e B)/\Delta$ for a given magnetic field B. The values reported in Table I correspond to an average value on the lowest magnetic fields data sets exploitable on wide enough temperature range (typically 8-10 T). The mass was found to be almost constant over the energy range studied, with a value of $0.245 \pm 0.015\, m_0$. This value is consistent with the values obtained in a higher (but overlapping) energy range.[13] A non-trivial field dependence was observed as the magnetic field was increased,[23] but is beyond the scope of the present paper where we aim at characterizing the (field-independent) hole Fermi surface. From the frequency F of the quantum oscillations discussed in the previous section, one can deduce the extremal Fermi surface cross-section in the momentum space, $CS = \pi k_F^2$ (where k_F is the Fermi wave vector), given by $CS = 2\pi e F/\hbar$. In the case of an energy-independent effective mass in the $B \parallel c$-axis configuration, the Fermi energy can be written $E_F = (\hbar^2 CS)/(2\pi m_h)$. Using this method, we have determined the Fermi energies reported in Table I, which define the energy range ($E_F \sim 20$ to 60 meV) probed by our experiment.

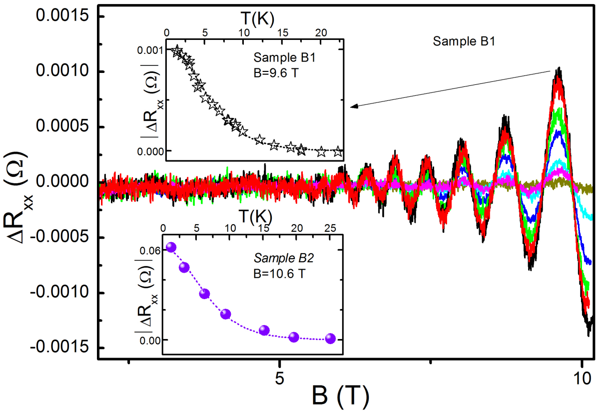

FIG. 2: (color online) Oscillatory magnetoresistance ΔR_{xx} versus total magnetic field parallel to the c-axis for different temperatures (1.4-17.5 K) in sample B1. Upper left inset: temperature dependence of ΔR_{xx} at a resistance extremum at $B = 9.6$ T. Lower left inset: temperature dependence of ΔR_{xx} at the resistance extremum at $B = 10.6$ T for sample B2.

III. HOLE FERMI SURFACE

A. Doping and angular dependences

In Fig. 3, we report the angular dependence of the FFT of the quantum oscillations in a color map for three samples with different hole concentrations.

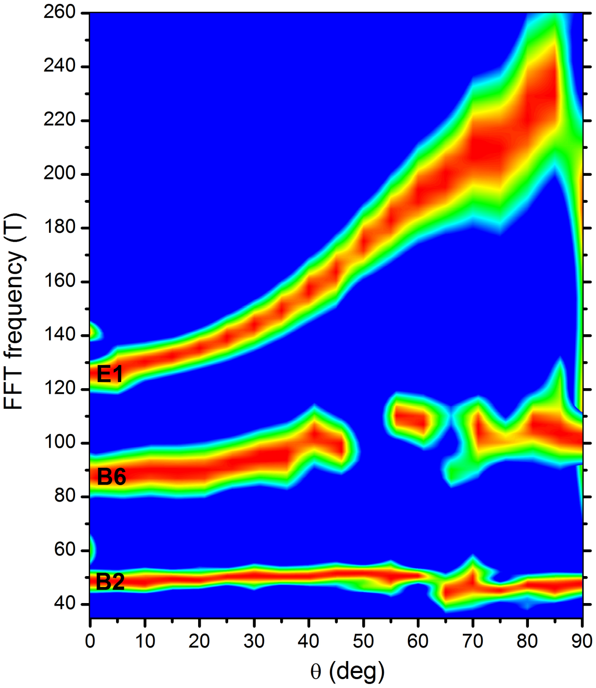

FIG. 3: (color online) Color plot : *Normalized* amplitude of the quantum oscillations $1/B$ Fourier transform as a function of the frequency and the tilt angle θ, for different samples. At each angle, the FFT signal is normalized to its maximal value (red color). The blue color corresponds to an intensity $\leq 70\%$ of the maximum value.

The displayed color map is a linear extrapolation of angular dependent data taken with a 5° step, where θ is the angle between the sample c-axis and the magnetic field. The FFT signals have been normalized to their maximum value for each angle to focus *only* on the angular dependence.[24] The frequency of the quantum oscillation is directly related to the cross-section of the Fermi surface in k-space. As the sample is rotated in the magnetic field, the angular dependence of this cross-section can be traced and related to the Fermi surface's geometry.

The overall observed non-monotonous behaviour of the frequency as a function of the tilt angle θ is characteristic of an anisotropic Fermi surface. At low energies ($E_F < 30$ meV) the angular dependence is rather mild, suggesting an almost isotropic Fermi surface. Anisotropy progressively develops with increasing Fermi energy and, for a frequency of 120 T at $\theta = 0°$, the $\theta = 90°$ frequency approximatively doubles. It should be noted that a $\cos\theta$ behavior, usually associated with a 2D system, was not observed in any sample even up to very high magnetic fields. This confirms that bulk states dominate both the transport and magnetization properties in samples of relatively large thicknesses. It is worth stressing that, as the system becomes anisotropic at high doping level, a *complete* angular dependence ($0° - 90°$ at least) is absolutely required to probe the dimensionality of the system (see the example of graphite, a very anisotropic 3D system showing a $\cos\theta$ behavior up to $\sim 70°$, in Ref. 25).

At variance with previous results obtained on n-type Bi_2Se_3 in the low energy region of the conduction band ($E_F < 30$ meV), the cross section cannot be reproduced accurately by assuming a purely ellipsoidal Fermi surface. A perhaps even more striking difference is the occurrence of a *downturn* in the angular dependence above a density-dependent angle (e.g. $\theta \sim 70°$ for sample B6). This demonstrates a "bag-shape" Fermi surface, where the cross section increases until it reaches the bag's diagonal axis from where it starts to decrease with further increasing the angle. A closer look at the low density data (sample B2) shows the downturn is also present on the apparently flat angular dependence (see section III B for a better representation). The intensity of the FFT signal (which can not be assessed in Fig. 3 because of the normalization) can to some extent also be informative. The raw FFT intensity reflects a severe drop in the oscillation amplitude where the downturn in frequency appears, for example around $\theta = 60°$ for sample B2 and B3. The FFT signal then clearly reappears from $\theta = 75°$ to $\theta = 90°$.[26] This drop in the amplitude may be correlated to the downturn in the angular dependence. The FS strong curvature change in this region probably leads to the loss of the phase coherence of the oscillations. We note that the downturn appears at higher angle for higher density. Finally, our data in the high energy limit (sample E1) are in good quantitative agreement with the previously reported SdH measurements in high hole density samples. In particular, oscillations are lost for specific θ ranges (see e.g. the sudden drop in frequency from $\theta = 90°$), corresponding to open orbits in the momentum space. We attribute these open orbits to the pipes emerging in the Fermi surface at high carrier density in the presence of trigonal warping.[27]

B. Theoretical model and discussion

In Fig. 4(a), we report the angular dependence of the quantum oscillation main frequency (FFT maximum) for different hole doping levels. These are the same data as the ones in Fig. 3 with additional samples at intermediate carrier concentrations. For each sample we computed the extremal cross-section of the Fermi surface in k-space from the $F(\theta)$ dependence. By assuming that the Fermi surface is closed and has rotational symmetry around the c-axis, the constant $k_\perp - k_z$ energy surface, where k_z is parallel to the trigonal axis of the Brillouin zone (c-axis) and $k_\perp = (k_x^2 + k_y^2)^{1/2}$ is in the plane perpendicular to k_z, was derived (not shown).[28] The θ angular dependence of the Fermi radius was then fitted by solving an analytical $E(k)$ dependence for each experimental Fermi energy reported in Table I. The empirical dispersion relation up to the k^4 order can be written as:[29]

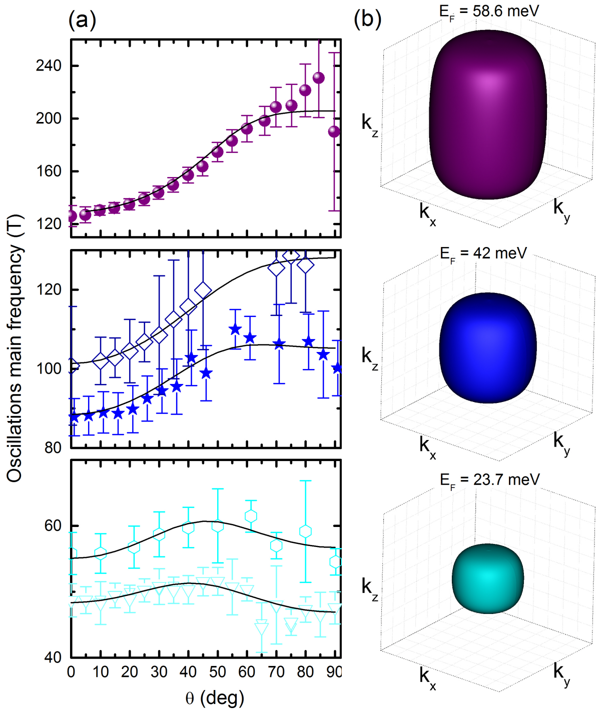

FIG. 4: (color online) (left panels) Quantum oscillation frequency as a function of the tilt angle θ for different carrier concentrations in the valence band. The error bar is defined to be the FFT width at 90% of the maximum signal. From bottom to top, sample B2 (SdH), B3 (SdH), B6 (dHvA), E2(dHvA) and E1(dHvA). Theoretical fits obtained by the analytical model of Eq.2 (see text) (solid lines). (Right panels) Fermi surfaces computed at $E_F = 23.7$, 42, and 58.6 meV.

$$E(k) = C_1 k_\perp^2 + C_2 k_z^2 + C_3 k_\perp^2 k_z^2 + C_4 k_\perp^4 + C_5 k_z^4 \\ + C_6 k_x (k_x^2 - 3k_y^2) + C_7 k_z k_y (k_y^2 - 3k_x^2) \quad (1)$$

From symmetry considerations, $E(k) = E(-k)$, which sets C_6=0. Neglecting non-parabolicity effects at low density leads to $C_4 = 0$ and $C_5 = 0$. The last term accounts for the trigonal warping of the Fermi surface, which we neglect in our first approach. The simplified expression we used can therefore be written as:

$$E(k) = C_1 k_\perp^2 + C_2 k_z^2 + C_3 k_\perp^2 k_z^2 \quad (2)$$

where the numerical values of the coefficients C_1, C_2 and C_3 are listed in the supplemental material, section III. The theoretical $F(\theta)$ dependencies are plotted as solid lines on top of the experimental points in Fig. 4(a) and three computed Fermi surfaces are shown in Fig. 4(b). At low energy (sample B2), the downturn of the oscillation frequency is well reproduced, and clearly results from the bag-shape nature of the Fermi surface. In this "squashed" ellipsoid the in-plane Fermi wave-vector k_F is longer than along the c-axis, leading to a negative anisotropy factor.[30] As the density increases, the shift of the downturn to higher angles is due to the elongation of the Fermi surface along the vertical axis. The anisotropy changes its sign, becomes positive, and grows continuously with E_F up to 1.4. It is illustrated by the oblong Fermi surface of sample E2 at $E_F = 58.6$ meV.

We now focus on the low energy limit valence band structure. In the presence of a strong spin-orbit coupling, the band inversion is expected to give rise to a camel-back structure, characterized by a local minimum at $k = 0$. This is reported in Figs. 5(a) and (b), where the dotted curves are the valence bands along $k_\perp$ and k_z obtained for the 4×4 Hamiltonian of Zhang *et al.*[2] and its original parameters. The camel-back is prominent with a band maximum occurring at finite $k_x \approx 0.07 \AA^{-1}$ and a $k_x = 0$ depth varying in theoretical works from about 80 meV[2] to 140 meV.[12]

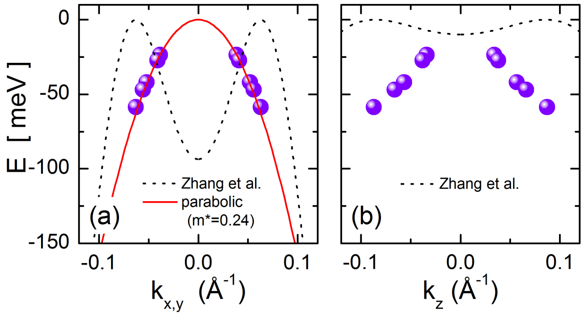

FIG. 5: (color online)(a) and (b) Valence band along $k_{x,y}$ and k_z respectively. Experimental data (dots), parabolic dispersion (solid lines) and camel-back model (dotted lines).

If the Fermi energy lies in the camel-back region, there should be no carriers around $k_\perp = 0$ and the Fermi surface should exhibit a "donut-like" shape. This should give two frequencies corresponding the the outer (maximal) and inner (minimal) orbits, as well as a single frequency of a much smaller value around $\theta = 90°$. Our observation of a single frequency around $\theta = 0°$ exhibiting moderate changes with the tilt angle suggests that there is no "camel-back" structure deeper than the lowest energy investigated (~ 23.7 meV). Let us now consider the case where the residual "camel back " depth is lower than ~ 23 meV . For our lowest Fermi energy, one would expect a single oscillation frequency at low angles, splitting into two frequencies above a certain angle. The low angle frequency would correspond to an orbit along the horizontal cross section of a "dumbbell-like" Fermi surface, and the two frequencies at high angles would correspond to the two extremal transversal section of the dumbbell. The size of the frequency splitting at $\theta = 90°$ is in this case related to the depth of the "camel-back" structure. At variance with these expectations, our measurements reveals that a *single* oscillation frequency persists up to $\theta = 90°$. This shows that no camel back structure can be observed at all within our experimental resolution (our

FFT full-width-half-maximum at $\theta = 90°$ is $\Delta F \sim 13$T).

The absence of the camel back structure can more generally be seen in figure 5(a), where the experimental points E_F vs $k_\perp$ are plotted, showing that camel-back structure is experimentally absent. The $k_\perp^2$ approximation used in Eq. 2 is justified by the good parabolic fit (red solid line) and the almost energy-independent mass measured experimentally with the temperature dependent studies $m_h = 0.24 m_0$. In Fig.5(b), we plot the experimental dispersion along k_z obtained from our simulations. Importantly, the k_z dispersion is far from being parabolic, E(k_z) showing a slower increase, in agreement with the observation made in previous ARPES measurements focusing on the $\Gamma - Z$ dispersion in the Brillouin zone.[31] In contrast to the $k_\perp$ dispersion, higher order terms (appearing in Eq. 1) are actually required. These conclusions are similar to the conduction band results obtained by Köhler *et al.*[29], where the $k_\perp^4$ and k_z^4 parameters were respectively $C_4 = 0$ and $C_5 \neq 0$, with $C_5 \neq 0$ and energy-dependent. We nevertheless did not consider this term in the data analysis as it improved the $F(\theta)$ curves plotted in Fig. 4(a) only slightly.

Our main observation that no camel-back structure is formed in the Bi_2Se_3 valence band is in qualitative agreement with other experimental work probing the bulk band structure of this compound.[10,32] This can be related to the recent conclusion of GW numerical computations that the band gap of Bi_2Se_3 is direct and reduced by the electron-electron interaction.[18,19]

IV. HOLE TRANSPORT TOWARDS THE QUANTUM LIMIT

For the lowest density samples (B2 and B3), magnetotransport experiments have been extended to high magnetic fields up to 30 T. Typical results are reported in Fig. 6 for sample B3. Simulations of the magnetoresistance were performed based on the simple phenomenological approach developed for the conduction band,[6,9] in which one considers a 3D electron gas with a large (spin-orbit-enhanced) spin gap $g^*_{eff}\mu_B B$, where g^* is the effective hole g-factor. As can be seen in Fig.6 the measured (background-removed) oscillations exhibit a *minimum* at $B \sim 22.5$ T, instead of the maximum expected from the $g^* = 0$ (no spin-splitting) simulation based on the low field oscillation frequency ($F = 55.8$ T). One could tentatively attribute this additional minimum to a spin-split feature only visible in the lowest Landau level/highest magnetic fields. The temperature dependence however shows that the energy gaps associated with the consecutive minima follow a continuous trend[21] and have therefore most likely the same origin. This suggests that Landau levels of different orbital and spin quantum numbers nearly coincide in energy, with consequently no visible spin splitting in the quantum oscillations. A similar scenario is observed in n-type Bi_2Se_3 where the spin gap is about twice the value of the cyclotron gap.[6,9] In such cases the quantum limit is repelled to higher magnetic fields due to a large field-dependent spin splitting shifting down the Landau levels energies.

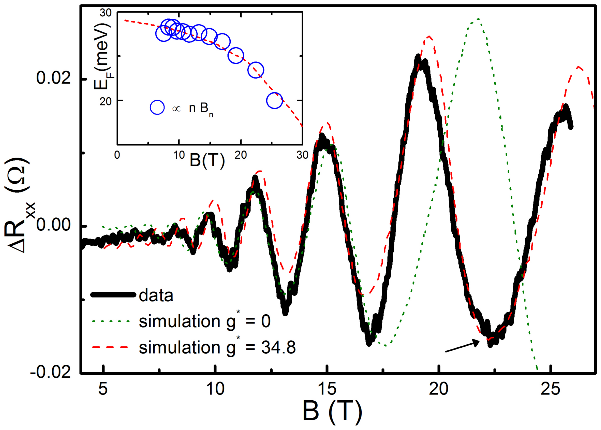

FIG. 6: (color online) Oscillatory magnetoresistance ΔR_{xx} versus total magnetic field at $T = 1.2$ K (solid line). Simulations for the $g^* = 0$ (dotted line) and $g^* = 34.8$ cases (dashed line). The arrow emphasizes the $B = 22.5$ T minimum. Inset: quantity proportional to the nB_n value (blue circle), and simulated Fermi energy as a function of the magnetic field for $g^* = 34.8$ (dashed line) (see text)

In the present case, when using the effective hole mass $m_h = 0.24 m_0$ determined in section II C, the best simulation is obtained for a g-factor of $g^* \sim 35$, for which spin-up and spin-down subbranches of the N and $N + 4$ Landau level coincide. As can be seen in Fig.6, the agreement with the data is not perfect (small dephasing can be seen at low magnetic fields) suggesting that some more complex field dependencies of the band parameters should be considered for a better description. The high value of the effective hole g-factor is nevertheless confirmed by simply analyzing the magnetoresistance peaks positions. The so-called "$1/B$ phase plots" show a severe deviation from linearity in high magnetic fields, which can be seen in the inset of Fig.6 where we focus on the product nB_n where n is an integer and B_n the magnetic field value corresponding to the n^{th} SdH extremum. SdH oscillations extrema occur when the ratio between the Fermi energy and the cyclotron gap ($\propto B$) equals $n/2$, and thus the product nB_n is proportional to the Fermi energy value. The y-axis value of the blue circles in the inset of Fig.6 is proportional to the measured nB_n value and show that the Fermi energy is reduced in high magnetic fields. This deviation is consistent with the Fermi energy drop expected in the presence of a high Zeeman energy, which is simulated by our model (dashed line). These observations stress, again, how crucial the contribution of the Zeeman energy is when conducting a phase oscillation analysis in such materials, in particular when searching for the (phase) signature of 2D surface carriers. Our results suggest that the effective g-factors could be similar in the bulk conduction and valence bands, which should be confirmed by a more direct measurement in p-type samples.

In conclusion, we have reported an energy-dependent study of the Bi_2Se_3 valence band based on quantum oscillations measurements in high magnetic fields and low temperatures. At low energies, a downturn observed in the oscillation frequency angular dependence reveals a bag-shaped closed hole Fermi surface. The absence of a spin-orbit-coupling induced "camel back" structure in the dispersion relation is further demonstrated. As the Fermi energy increases, anisotropy rapidly develops in the hole Fermi surface.

We aknowledge support from EC-EuroMagNetII-228043. The material synthesis work was supported by the National Science Foundation (NSF) under grant number DMR-1255607.

---

[1] S. K. Mishra, S. Satpathy, and O. Jepsen, Journal of Physics: Condensed Matter **9**, 461 (1997).

[2] H. Zhang, C.-X. Liu, X.-L. Qi, X. Dai, Z. Fang, and S.-C. Zhang, Nat Phys **5**, 438 (2009), ISSN 1745-2473.

[3] Y. Xia, D. Qian, D. Hsieh, L. Wray, A. Pal, H. Lin, A. Bansil, D. Grauer, Y. S. Hor, R. J. Cava, et al., Nat Phys **5**, 398 (2009), ISSN 1745-2473.

[4] Y. L. Chen, J. G. Analytis, J.-H. Chu, Z. K. Liu, S.-K. Mo, X. L. Qi, H. J. Zhang, D. H. Lu, X. Dai, Z. Fang, et al., Science **325**, 178 (2009).

[5] L. Fu and C. L. Kane, Phys. Rev. B **76**, 045302 (2007).

[6] H. Köhler, Phys. stat.sol. (b) **58**, 91 (1973).

[7] K. Eto, Z. Ren, A. A. Taskin, K. Segawa, and Y. Ando, Phys. Rev. B **81**, 195309 (2010), URL `http://link.aps.org/doi/10.1103/PhysRevB.81.195309`.

[8] B. Fauqué, N. P. Butch, P. Syers, J. Paglione, S. Wiedmann, A. Collaudin, B. Grena, U. Zeitler, and K. Behnia, Phys. Rev. B **87**, 035133 (2013), URL `http://link.aps.org/doi/10.1103/PhysRevB.87.035133`.

[9] S. Mukhopadhyay, S. Krämer, H. Mayaffre, H. F. Legg, M. Orlita, C. Berthier, M. Horvatić, G. Martinez, M. Potemski, B. A. Piot, et al., Phys. Rev. B **91**, 081105 (2015), URL `http://link.aps.org/doi/10.1103/PhysRevB.91.081105`.

[10] M. Orlita, B. A. Piot, G. Martinez, N. K. S. Kumar, C. Faugeras, M. Potemski, C. Michel, E. M. Hankiewicz, T. Brauner, i. c. v. Drašar, et al., Phys. Rev. Lett. **114**, 186401 (2015), URL `http://link.aps.org/doi/10.1103/PhysRevLett.114.186401`.

[11] Y. S. Hor, A. Richardella, P. Roushan, Y. Xia, J. G. Checkelsky, A. Yazdani, M. Z. Hasan, N. P. Ong, and R. J. Cava, Phys. Rev. B **79**, 195208 (2009).

[12] D. Hsieh, Y. Xia, D. Qian, L. Wray, J. H. Dil, F. Meier, J. Osterwalder, L. Patthey, J. G. Checkelsky, N. P. Ong, et al., Nature **460**, 1101 (2009), ISSN 0028-0836.

[13] Y.-B. Gao, B. He, D. Parker, I. Androulakis, and J. P. Heremans, Phys. Rev. B **90**, 125204 (2014), URL `http://link.aps.org/doi/10.1103/PhysRevB.90.125204`.

[14] P. Larson, V. A. Greanya, W. C. Tonjes, R. Liu, S. D. Mahanti, and C. G. Olson, Phys. Rev. B **65**, 085108 (2002), URL `http://link.aps.org/doi/10.1103/PhysRevB.65.085108`.

[15] D. Parker and D. J. Singh, Phys. Rev. X **1**, 021005 (2011), URL `http://link.aps.org/doi/10.1103/PhysRevX.1.021005`.

[16] K. W. Post, B. C. Chapler, L. He, X. Kou, K. L. Wang, and D. N. Basov, Phys. Rev. B **88**, 075121 (2013), URL `http://link.aps.org/doi/10.1103/PhysRevB.88.075121`.

[17] L. J. Sandilands, A. A. Reijnders, M. Kriener, K. Segawa, S. Sasaki, Y. Ando, and K. S. Burch, Phys. Rev. B **90**, 094503 (2014), URL `http://link.aps.org/doi/10.1103/PhysRevB.90.094503`.

[18] O. V. Yazyev, E. Kioupakis, J. E. Moore, and S. G. Louie, Phys. Rev. B **85**, 161101 (2012).

[19] I. Aguilera, C. Friedrich, G. Bihlmayer, and S. Blügel, Phys. Rev. B **88**, 045206 (2013), URL `http://link.aps.org/doi/10.1103/PhysRevB.88.045206`.

[20] Z. Wang, T. Lin, P. Wei, X. Liu, R. Dumas, K. Liu, and J. Shi, Applied Physics Letters **97**, 042112 (2010).

[21] A complete description of the transport properties is presented in the supplemental material, section I.

[22] I. Lifshitz and A. Kosevich, Zh. Eksp. Teor . Fiz. **29**, 730 (1955), [Sov. Phys. JETP 2, 636 (1956)].

[23] See the supplemental material, section I.B.

[24] Details on the FFT procedure can be found in the supplemental material, section II.A.

[25] J. M. Schneider, B. A. Piot, I. Sheikin, and D. K. Maude, Phys. Rev. Lett. **108**, 117401 (2012), URL `http://link.aps.org/doi/10.1103/PhysRevLett.108.117401`.

[26] See the supplemental material, section II.B. for more details.

[27] See the supplemental material, section II.C. for more details.

[28] F. M. Mueller, Phys. Rev. **148**, 636 (1966), URL `http://link.aps.org/doi/10.1103/PhysRev.148.636`.

[29] H. Köhler and H. Fischer, Phys. Stat. Sol. (b) pp. 349–357 (1975).

[30] The evolution of the anisotropy as a function of the Fermi energy is reported in the supplemental material, section III.

[31] V. A. Greanya, W. C. Tonjes, R. Liu, C. G. Olson, D.-Y. Chung, and M. G. Kanatzidis, Journal of Applied Physics **92**, 6658 (2002), URL `http://scitation.aip.org/content/aip/journal/jap/92/11/10.1063/1.1517748`.

[32] I. A. Nechaev, R. C. Hatch, M. Bianchi, D. Guan, C. Friedrich, I. Aguilera, J. L. Mi, B. B. Iversen, S. Blügel, P. Hofmann, et al., Phys. Rev. B **87**, 121111 (2013), URL `http://link.aps.org/doi/10.1103/PhysRevB.87.121111`.